*Supporting Information for*

# Non-Hermitian Singularities in Colloidal Plasmon–Exciton Interactions

O. B. Orhan,[1,†] N. Polat,[1,2,†,*] M. M. Khan,[2] S. K. Ozdemir,[2,*] and S. Balci[1,*]

[1]Department of Photonics, Izmir Institute of Technology, Izmir 35430, Turkey

[2]Department of Electrical and Computer Engineering, Saint Louis University, St. Louis, MO, 63103 USA

[†]These authors contributed equally

[*]E-mails: sinanbalci@iyte.edu.tr, nahit.polat@slu.edu, and sahin.ozdemir@slu.edu

**TABLE OF CONTENTS:**

**REFERENCES**

## S1. Chemicals and materials

All chemicals utilized in this study were obtained from commercial sources and used without further purification. Specifically, hydrogen tetrachloroaurate (III) trihydrate ($HAuCl_4 \cdot 3H_2O$, purity ≥ 99.9%), hexadecyltrimethylammonium bromide (CTAB, H5882, purity ≥ 98%), hexadecyltrimethylammonium chloride (CTAC, 52366, purity ≥ 98%), and ascorbic acid were all purchased from Sigma-Aldrich. Silver nitrate ($AgNO_3$, purity ≥ 99.8%) was purchased from ISOLAB Chemicals. Sodium borohydride ($NaBH_4$, 480866, purity ≥ 99.9%) was purchased from Merck. A cyanine dye, utilized as a J-aggregate dye, 5,5′,6,6′-tetrachloride (4-sulfobutyl) benzimidazolocarbo-cyanine (TDBC) was obtained from FEW Chemicals. Milli−Q water (18.2 MΩ·cm resistivity at 25 ℃) was used in all the experiments.

## S2. Synthesis of gold nanorods

Gold nanorods were synthesized using the seed-mediated growth protocol previously reported by Nikoobakht et al.[1]

### S2.1. Synthesis of gold seed solution

0.364 g of CTAB powder was dissolved in 5 mL of Milli-Q water under stirring at 200 rpm and 40 ℃. After complete dissolution of CTAB, the solution was cooled to room temperature, and 5 mL of 0.0005 M aqueous $HAuCl_4$ solution was added. The colorless solution turned yellow and was stirred for 5 minutes. Subsequently, 0.6 mL of 0.01 M ice-cold $NaBH_4$ solution was added while stirring at 600 rpm, resulting in a brownish color indicative of seed particle formation. The seed solution was aged for 2 hours to ensure complete decomposition of excess $NaBH_4$.[2]

**S2.2. Growth of gold nanorods with LSPR between 660 and 800 nm**

Initially, 0.364 g of CTAB powder was dissolved in 9.5 mL of Milli-Q water under constant stirring at 200 rpm and 40 °C. After complete dissolution, the solution was cooled to room temperature, followed by the addition of 0.5 mL of 0.01 M aqueous $HAuCl_4$ and varying volumes (35, 50, or 100 µL) of 0.01 M $AgNO_3$ solution. The colorless solution turned orange-yellow and was stirred at 200 rpm for 20 minutes to ensure effective complexation between the gold salt and surfactant molecules.[3] Subsequently, 55 µL of 0.1 M ascorbic acid solution was added to the mixture, turning it colorless and indicating the reduction of $Au^{3+}$ to $Au^{+}$.[4] In the final step, 15 µL of the prepared seed solution was added to the growth solution. The growth solution was then left undisturbed in a 27 °C water bath for 1 hour. Upon completion of nanorod growth, the solution exhibited either a blue or light pinkish-brown color, depending on the concentration of $AgNO_3$. After synthesis, the NR solution was immediately centrifugation at 15000 rpm for 10 minutes to remove excess reagents.

**S2.3. Growth of gold nanorods with LSPR above 800 nm**

To synthesize longer NRs, various methods have been reported, including two-component surfactant systems and hydroquinone (HQ)-assisted processes.[1,5,6] We employed the HQ-based method to synthesize long NRs. To achieve this objective, 0.364 g of CTAB powder was dissolved in 10 mL of Milli-Q water under constant stirring at 200 rpm and 40 °C. After complete dissolution, the solution was cooled to room temperature, followed by addition of 50 µL of 0.1 M aqueous $HAuCl_4$ and 50 µL of 0.1 M $AgNO_3$ solution. The colorless solution turned orange-yellow and was stirred at 200 rpm for 20 minutes to ensure effective complexation between the gold salt and surfactant molecules. Subsequently, 500 µL of 0.1 or 0.2 M HQ solution was added, resulting in a

colorless mixture. In the final step, 240 µL of the prepared seed solution was introduced. The growth solution was then left undisturbed in a 27 ℃ water bath overnight. Upon completion, the solution exhibited a brown coloration, with the longitudinal plasmon resonance wavelength ranging from 900 to 1100 nm, depending on the HQ concentration in the growth solution. The NR solution was immediately centrifuged at 15000 rpm for 10 minutes to remove excess reagents.

### S2.4. Purification of gold nanorods

It is well-known that the standard seed-mediated synthesis of gold NRs produces a small fraction of spherical gold nanoparticle byproducts.[1,7,8] To address this issue and ensure that the final core-shell structures consist exclusively of purified gold NRs, a shape-selective centrifugal protocol was employed.[9,10] We observed that under specific centrifugal conditions, NRs remain dispersed in the supernatant due to their lower sedimentation rate compared to spherical nanoparticles. Based on this, a cascade centrifugation method was performed following isolation of the gold NRs from the growth medium. The NR solution was centrifuged at 6000 rpm for 15 minutes, after which the supernatant-confirmed to contain NRs by the presence of a LSPR band in the extinction spectra-was collected. The NR concentration was then adjusted to a defined value on the intensity of the LSPR peak.

## S3. Silver shell growth on gold nanorods

A well-established method from the literature was employed.[11,12] Prior to the coating process, the gold NRs were centrifuged twice at 15000 rpm for 10 minutes to thoroughly remove residual

CTAB from the medium. A 2.25 mL aliquot of the NR solution (with the LSPR peak absorbance adjusted to approximately 1) was added to 3.75 mL of 0.08 M CTAC solution and gently mixed using a vortex stirrer. Once the solution appeared homogeneous, varying volumes of 0.01 M $AgNO_3$ (80, 120, 150, 200, and 500 μL) and 0.1 M ascorbic acid (40, 60, 75, 100, and 250 μL) were added and gently mixed. The mixture was then left undisturbed in a water bath at 65 ℃ for 3 hours to allow for silver shell growth. The resulting core-shell nanostructures were centrifuged at 10000 rpm for 10 minutes to remove excess reactants, and the pellet was subsequently redispersed in water.

**S4. Assembly of J-aggregates on plasmonic nanocrystals**

A self-assembly method was employed to synthesize hybrid plasmon-exciton nanocrystals.[13] Varying volumes of 0.1 mM aqueous TDBC solution were mixed with 1 mL of plasmonic nanoparticle solution, and time-dependent extinction measurements were performed. These measurements indicated that the self-assembly of J-aggregates onto the plasmonic nanocrystals was completed within approximately 45 minutes (See **Fig. S7**). Each hybrid nanoparticle solution was then aliquoted into separate vials, placed vertically, and left undisturbed overnight in a dark environment to promote the self-organization of dye molecules. The optical properties of the resulting hybrid structures were subsequently measured.

**S5. Refractive index sensing experiments**

The refractive index sensing of plasmon-exciton hybrid nanocuboids was carried out following the procedure described in a previous study.[14] Dimethyl sulfoxide (DMSO) was used as a co-solvent to modulate the refractive index of the aqueous dispersion, due to its relatively high refractive

index. The DMSO concentration was systematically varied from 2% to 50% (volume) of the total solvent mixture, corresponding to a refractive index range of 1.339 to 1.406. Extinction spectra were recorded for each composition. It is crucial to highlight that DMSO concentrations beyond this range led to degradation of the hybrid plasmon-exciton nanoparticles, attributed to the exothermic interaction between water and DMSO.

**S6. Optical and structural characterization**

All characterization measurements were conducted under ambient conditions. Optical extinction spectra of the gold nanorods, core-shell structures, and hybrid plasmon-exciton hybrid nanoparticles were acquired using a polymeric cuvette with a 1 cm optical path length. A balanced deuterium-tungsten halogen light source (DH2000-BAL, Ocean Optics) and a fiber-coupled spectrometer (USB4000, Ocean Optics) were employed for extinction measurements. The morphology of the gold nanorods was analyzed using a Scanning Transmission Electron Microscope (STEM) (SEM; Quanta 250, FEI, Hillsboro, USA). For STEM imaging, samples were prepared by drop-casting the nanoparticle solutions onto 200-mesh copper grids.

**S7. FDTD simulations**

Finite-Difference Time-Domain (FDTD) simulations of a single gold nanorod and an Au@Ag nanocuboid were performed using Lumerical software. The optical constants ($n$ and $k$) for gold and silver were derived from the Palik dataset.[15] For the TDBC dye, a Lorentz oscillator model[16] was employed, using a full width at half maximum (FWHM) of 32 meV. The optical responses of the isolated gold nanorod and the Au@Ag nanocuboid were subsequently analyzed.

## S8. Theoretical model of the Non-Hermitian plasmon-exciton interaction

We model the coupled plasmon–exciton system using an effective non-Hermitian Hamiltonian of the form

$$H_{eff} = \begin{pmatrix} \omega_{pl} + i\frac{\gamma_{pl}}{2} & \sqrt{N}g \\ \sqrt{N}g & \omega_{ex} + i\frac{\gamma_{ex}}{2} \end{pmatrix}, \tag{S1}$$

where $\omega_{pl}$ and $\omega_{ex}$ denote the bare resonance frequencies of the plasmonic and excitonic modes, respectively. The corresponding damping rates are given by $\gamma_{pl}$ and $\gamma_{ex}$, and $\sqrt{N}g$ represents the collective coupling strength, where $N$ denotes the number of coupled excitonic molecules and $g$ is the single-particle interaction strength.

The complex eigenvalues of $H_{eff}$ are found as

$$\omega_{\pm} = \frac{\omega_{pl} + \omega_{ex}}{2} + i\frac{\gamma_{pl} + \gamma_{ex}}{4} \pm \frac{1}{2}\sqrt{\left(\omega_{pl} - \omega_{ex} + i\frac{\gamma_{pl} - \gamma_{ex}}{2}\right)^2 + 4Ng^2}. \tag{S2}$$

Assuming zero frequency detuning between plasmonic and excitonic modes, i.e., $\omega_{pl} = \omega_{ex} = \omega_0$, and defining damping rate imbalance between the plasmonic and excitonic modes as $\Gamma = \gamma_{pl} - \gamma_{ex}$, we can simplify Eq. (S2) to

$$\omega_{\pm} = \omega_0 + i\frac{\Gamma + 2\gamma_{ex}}{4} \pm \frac{1}{2}\sqrt{4Ng^2 - \left(\frac{\Gamma}{2}\right)^2}. \tag{S3}$$

When the square-root term vanishes, that is

$$4\sqrt{N}g = \pm\Gamma \tag{S4}$$

an EP emerges at the complex eigenfrequency $\omega_{\pm} = \omega_{EP} = \omega_0 + i(\Gamma + 2\gamma_{ex})/4$. This EP point marks the transition point between the weak coupling regime where $4\sqrt{N}g \ll \Gamma$ and the intermediate coupling regime where $4\sqrt{N}g \gg \Gamma$ and $\sqrt{N}g < \gamma_{pl}, \gamma_{ex}$. Similarly, the system said to

be in the strong coupling regime when $\sqrt{N}g > \gamma_{pl}, \gamma_{ex}$. In the strong coupling regime, the plasmonic and excitonic modes hybridizes leading to two supermodes with complex frequencies $\omega_{\pm}$ which are well-separated in the real part of their complex frequencies (i.e., $\Delta\Omega = \omega_{+} - \omega_{-} = \sqrt{4Ng^2 - (\Gamma/2)^2}$, leading to emergence of split modes in the extinction spectra (i.e., well-separated upper and lower polaritonic branches). This regime also is identified with the emergence of coherent Rabi oscillations. In the weak coupling regime, the modes differ in the imaginary part of their complex frequencies which appear as a single resonance with broaden lineshape in the extinction spectra. The intermediate coupling regime marks the transition zone from strong to weak coupling and is characterized by Fano-like lineshapes. In this regime, the split modes are not separated as well as the strong coupling regime, and thus coherent Rabi oscillations are not observed or decays very fast implying the non-Hermitian dynamics becoming dominant.

**S8.1. Adding small perturbations to effective non-Hermitian Hamiltonian**

In this study, we use our colloidal plexitonic system as a refractive index sensor. Refractive index changes in our system affect the diagonal elements of the effective Hamiltonian $H_{eff}$ given in Eq. (S1). Such perturbations can be incorporated into $H_{eff}$ leading to the perturbed Hamiltonian $H'$:

$$H' = \begin{bmatrix} \omega_{pl} + \epsilon_1 + i\frac{\gamma_{pl}}{2} & \sqrt{N}g \\ \sqrt{N}g & \omega_{ex} + \epsilon_2 + i\frac{\gamma_{ex}}{2} \end{bmatrix}, \tag{S5}$$

where $\epsilon_1$ and $\epsilon_2$ denote the effect of the refractive index change on the plasmonic and excitonic resonance frequencies, respectively. Such perturbations (i.e., refractive index of colloidal solution) effectively change the complex frequencies of the plasmonic and excitonic modes. The eigenvalues of the perturbed Hamiltonian $H'$ are given by

$$\omega_{\pm} = \frac{\omega_{pl} + \omega_{ex}}{2} + \frac{\epsilon_1 + \epsilon_2}{2} + i\frac{\gamma_{pl} + \gamma_{ex}}{4} \pm \frac{1}{2}\sqrt{\left(\omega_{pl} - \omega_{ex} + \epsilon_1 - \epsilon_2 + i\frac{\gamma_{pl} - \gamma_{ex}}{2}\right)^2 + 4Ng^2} \quad \text{(S6)}$$

Assuming that before the refractive index perturbation the plasmon-exciton frequency detuning is zero ($\omega_{pl} = \omega_{ex} = \omega_0$ ) and defining the damping rate asymmetry as $\Gamma = \gamma_{pl} - \gamma_{ex}$, we rewrite the eigenvalues as

$$\omega_{\pm} = \omega_0 + \epsilon_c + i\frac{\Gamma + 2\gamma_{ex}}{4} \pm \frac{1}{2}\sqrt{\left(\delta + i\frac{\Gamma}{2}\right)^2 + 4Ng^2}. \quad \text{(S7)}$$

where $\epsilon_c = \frac{\epsilon_1 + \epsilon_2}{2}$ and $\delta = \epsilon_1 - \epsilon_2$. Then the amount of mode splitting is found as $\Delta\Omega = \omega_+ - \omega_-$

$$\Delta\Omega = \sqrt{\left(\delta + i\frac{\Gamma}{2}\right)^2 + 4Ng^2}. \quad \text{(S8)}$$

**S8.2. Eigenvalue splitting at EP**

The eigenvalue splitting is obtained by expanding square-root term in Eq.(S8)

$$\Delta\Omega = \sqrt{\delta^2 + i\delta\Gamma - \frac{\Gamma^2}{4} + 4Ng^2}. \quad \text{(S9)}$$

At the exceptional point, the coupling precisely compensates the damping-rate asymmetry, as per Eq.(S4). Consequently, the EP condition-related terms within the square root vanish, leading to

$$\Delta\Omega = \sqrt{\delta^2 + i\delta\Gamma}. \quad \text{(S10)}$$

Equation (S10) can be conveniently rewritten by factoring out the dominant contribution in the small-perturbation limit $\delta \ll \Gamma$. Specifically, extracting the term $\sqrt{i\Gamma\delta}$ yields

$$\Delta\Omega = \sqrt{i\Gamma\delta}\sqrt{1 - i\frac{\delta}{\Gamma}}. \tag{S11}$$

To obtain an explicit asymptotic expression, we expand the expression in Eq.(S11) as $\sqrt{1+x} = 1 + {}^{x}/_{2} - {}^{x^2}/_{8} + O(x^3)$ with $x \equiv -i\frac{\delta}{\Gamma}$ and $\frac{\delta}{\Gamma} \ll 1$ leading to

$$\sqrt{1 - i\frac{\delta}{\Gamma}} = 1 - i\frac{\delta}{2\Gamma} + \frac{1}{8}\left(\frac{\delta}{\Gamma}\right)^2 + O\left(\left(\frac{\delta}{\Gamma}\right)^3\right). \tag{S12}$$

Substituting Eq.(S12) into Eq.(S11) and retaining terms up to first order in $\delta/\Gamma$, we obtain the following approximate expression for the eigenvalue splitting near the EP:

$$\Delta\Omega \approx \sqrt{\delta}\sqrt{i\Gamma}\left(1 - i\frac{\delta}{2\Gamma}\right) \tag{S13}$$

Using the principal-branch representation of complex square root, $\sqrt{i\Gamma} = \sqrt{\Gamma/2}\,(1+i)$, the expression in Eq.(S13) can be further decomposed into its real and imaginary components, yielding

$$\Delta\Omega \approx \sqrt{\delta}\sqrt{\frac{\Gamma}{2}} + i\sqrt{\delta}\sqrt{\frac{\Gamma}{2}} \tag{S14}$$

which shows that the real part of the eigenvalue splitting follows a square-root dependence on the perturbation strength,

$$\mathrm{Re}(\Delta\Omega) \propto \sqrt{\delta} \tag{S15}$$

**S8.3. Eigenvalue splitting in the weak-coupling regime**

We now consider the weak-coupling regime, defined by $4\sqrt{N}g \ll \Gamma$, where dissipative effects dominate over plasmon-exciton coupling. Expending square root terms in Eq.(S8), we find

$$\Delta\Omega = \sqrt{\delta^2 + i\delta\Gamma - \frac{\Gamma^2}{4} + 4Ng^2}. \tag{S16}$$

In the weak-coupling regime, the dominant contribution arises from the dissipative term proportional to $\Gamma^2$. We then can rewrite Eq.(S16) as

$$\Delta\Omega = \mathrm{i}\frac{\Gamma}{2}\sqrt{1-\left(\frac{4\delta^2}{\Gamma^2}+\frac{i4\delta}{\Gamma}+\frac{16Ng^2}{\Gamma^2}\right)} \tag{S17}$$

In the weak-coupling regime, both $\delta/\Gamma$ and $g/\Gamma$ are small parameters, and thus the square-root term can be expanded using $\sqrt{1+x} \approx 1+\frac{x}{2}$ with $|x| \ll 1$ and $x \equiv -\left(\frac{4\delta^2}{\Gamma^2}+\frac{i4\delta}{\Gamma}+\frac{16Ng^2}{\Gamma^2}\right)$, yielding

$$\sqrt{1-\left(\frac{4\delta^2}{\Gamma^2}+\frac{i4\delta}{\Gamma}+\frac{16Ng^2}{\Gamma^2}\right)} \approx 1-\frac{1}{2}\left(\frac{4\delta^2}{\Gamma^2}+\frac{i4\delta}{\Gamma}+\frac{16Ng^2}{\Gamma^2}\right). \tag{S18}$$

Substituting Eq.(S18) back into Eq.(S17), we obtain the splitting as

$$\Delta\Omega \approx \mathrm{i}\frac{\Gamma}{2}\left(1-\frac{1}{2}\left(\frac{4\delta^2}{\Gamma^2}+\frac{i4\delta}{\Gamma}+\frac{16Ng^2}{\Gamma^2}\right)\right). \tag{S19}$$

Separating Eq.(S19) into its real and imaginary parts and retaining leading-order terms in the weak-coupling limit yields

$$\Delta\Omega \approx \delta+\mathrm{i}\left(\frac{\Gamma}{2}-\frac{\delta^2}{\Gamma}-\frac{4Ng^2}{\Gamma}\right). \tag{S20}$$

Eq. (S20) reveals that in the weak-coupling regime the real part of the eigenvalue splitting exhibits a linear dependence on the perturbation strength,

$$\mathrm{Re}(\Delta\Omega) \propto \delta \tag{S21}$$

**S8.4. Eigenvalue splitting in strong-coupling regime**

We next consider the strong coupling regime, $4\sqrt{N}g \gg \Gamma$. The eigenvalue splitting is obtained by expanding the square root term in Eq.(S8)

$$\Delta\Omega = \sqrt{\delta^2 + i\delta\Gamma - \frac{\Gamma^2}{4} + 4Ng^2}. \tag{S22}$$

In this limit, the coupling term $4Ng^2$ dominates the square root expression governing the complex eigenvalue splitting which allows us to write the splitting as

$$\Delta\Omega = 2\sqrt{\mathrm{N}}g\sqrt{1 + \frac{\delta^2}{4Ng^2} + \frac{i\delta\Gamma}{4Ng^2} - \frac{\Gamma^2}{16Ng^2}} \tag{S23}$$

Accordingly, for $\delta/2\sqrt{N}g \ll 1$ and $\Gamma/4\sqrt{N}g \ll 1$, we can use $\sqrt{1+x} \approx 1 + x/2$ , for $|x| \ll 1$, to rewrite Eq. (S23) as

$$\Delta\Omega \approx 2\sqrt{\mathrm{N}}g\left(1 + \frac{1}{2}\left(\frac{\delta^2}{4Ng^2} - \frac{\Gamma^2}{16Ng^2} + \frac{i\delta\Gamma}{4Ng^2}\right)\right), \tag{S24}$$

Accordingly, the real part of the eigenvalue splitting reads

$$\mathrm{Re}(\Delta\Omega) \approx 2\sqrt{\mathrm{N}}g + \frac{\delta^2}{4\sqrt{\mathrm{N}}g} - \frac{\Gamma^2}{16\sqrt{\mathrm{N}}g} \tag{S25}$$

In this expression, the $2\sqrt{\mathrm{N}}g$ corresponds to the eigenvalue splitting of unperturbed Hamiltonian ($\Delta\Omega_0$). Because $\Gamma^2/16\sqrt{\mathrm{N}}g \ll 1$ in the strong coupling regime, the damping-induced correction constitutes only a small offset to the dominant splitting. Thus, the deviation of the real-part eigenvalue splitting from its unperturbed value exhibits a quadratic dependence,

$$\mathrm{Re}(\Delta\Omega) - \mathrm{Re}(\Delta\Omega_0) \propto \delta^2. \tag{S26}$$

**S9. Coupled-oscillator model for spectral analysis**

To quantitatively analyze the hybrid plasmon–exciton modes observed in the extinction spectra, the system was modeled using a classical coupled-oscillator formalism. In this framework, the

interaction between the localized surface plasmon resonance (LSPR) of the bimetallic nanocuboids and the excitonic transition of the TDBC J-aggregate dye is described by the following set of linear equations[17]:

$$\begin{pmatrix} \omega_{pl} - \omega - \frac{i\gamma_{pl}}{2} & g \\ g & \omega_{ex} - \omega - \frac{i\gamma_{ex}}{2} \end{pmatrix} \begin{pmatrix} x_{pl} \\ x_{ex} \end{pmatrix} = i \begin{pmatrix} f_{pl} \\ f_{ex} \end{pmatrix}. \quad \text{(S27)}$$

Here, $\omega_{pl}$ and $\omega_{ex}$ represent the uncoupled resonance frequencies of the plasmonic and excitonic modes. The parameters $\gamma_{pl}$ and $\gamma_{ex}$ denote their respective damping rates, accounting for radiative and non-radiative losses. The parameter g describes the coherent coupling strength between the oscillators. The external driving amplitudes $f_{pl}$ and $f_{ex}$ represent the excitation efficiencies of the plasmonic and excitonic modes under incident optical illumination. In our model, the incident field is assumed to couple predominantly to the plasmonic mode, and therefore the direct excitation of the excitonic oscillator is neglected ($f_{ex} = 0$). Consequently, the excitonic mode is excited indirectly through its coupling to the plasmonic oscillator. The complex amplitudes $x_{pl}$ and $x_{ex}$ correspond to the steady state modal responses of the plasmonic and excitonic oscillators when the system is driven at frequency $\omega$.

**S9.1 Analytical Solution**

Solving Eq.(S27) yields the modal amplitudes

$$\mathrm{x}_{pl}(\omega) = \frac{i\left[\left(\omega_{ex} - \omega - \frac{i\gamma_{ex}}{2}\right) f_{pl} - g f_{ex}\right]}{\left(\omega_{pl} - \omega - \frac{i\gamma_{pl}}{2}\right)\left(\omega_{ex} - \omega - \frac{i\gamma_{ex}}{2}\right) - g^2} \quad \text{(S28)}$$

$$\mathrm{x}_{ex}(\omega) = \frac{i\left[\left(\omega_{pl} - \omega - \frac{i\gamma_{pl}}{2}\right) f_{ex} - g f_{pl}\right]}{(\omega_{pl} - \omega - \frac{i\gamma_{pl}}{2})(\omega_{ex} - \omega - \frac{i\gamma_{ex}}{2}) - g^2} \tag{S29}$$

The denominator

$$\mathrm{D}(\omega) = (\omega_{pl} - \omega - \frac{i\gamma_{pl}}{2})(\omega_{ex} - \omega - \frac{i\gamma_{ex}}{2}) - g^2 \tag{S30}$$

determines the hybridized eigenmodes of the system. Its poles correspond to the upper and lower polariton branches originating from plasmon–exciton coupling. This analytical form not only describes the spectral response in the weak and intermediate coupling regimes but also enables the identification of exceptional points (EPs) and the evaluation of the resulting enhanced responsivity to external perturbations.

**S9.2 Relation to the measured spectrum**

In the present system, the experimentally measured extinction spectrum is primarily governed by the plasmonic response of the nanocuboids, which couples strongly to the incident optical field. Consequently, the spectral intensity is proportional to the squared magnitude of the plasmonic oscillator amplitude:

$$I(\omega) \propto \left|x_{pl}(\omega)\right|^2 \tag{S31}$$

where $x_{pl}$ represents the response of the plasmonic mode associated with LSPR of the nanocuboids. In the coupled-oscillator model, the second oscillator amplitude $x_{ex}$ describes the

excitonic mode associated with the optical transition of the TDBC J-aggregate molecules. Although the excitonic oscillator does not directly dominate the far-field optical signal, it modifies the plasmonic response through coherent coupling, thereby shaping the observed spectral features. This quantity captures the spectral redistribution of the plasmon resonance induced by its interaction with the excitonic transition. Because the plasmonic resonance is spectrally broad while the excitonic resonance is narrow, the interference between these two oscillators produces an asymmetric spectral profile. Depending on the coupling strength and the detuning between the two modes, the resulting line shape can evolve from a slightly distorted single resonance (weak coupling) to linewidth modification near the exceptional point, and eventually to a clearly resolved doublet corresponding to the upper and lower polariton branches in the strong-coupling regime.

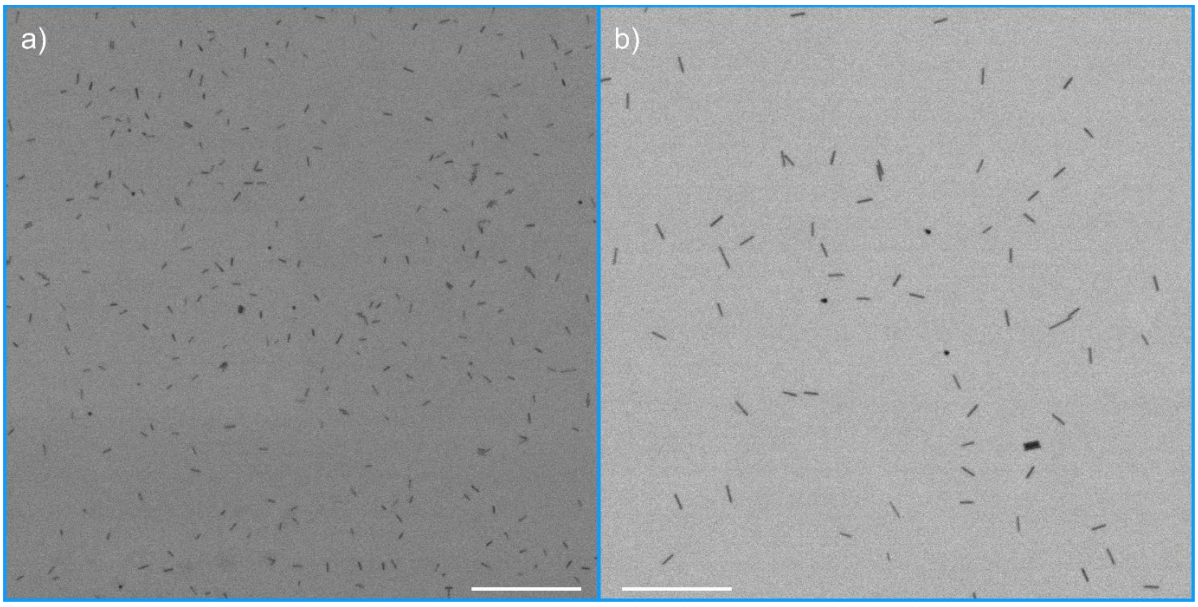


**Figure S1. STEM images of gold nanorods.** Large-area STEM images of the synthesized gold nanorods confirm that the majority of the particles exhibit a rod-like morphology. Image (a) shows nanorods with a mean aspect ratio of 5.5, while image (b) displays nanorods with a mean aspect ratio of 7. White horizontal lines represent the scale bars of 500 nm.

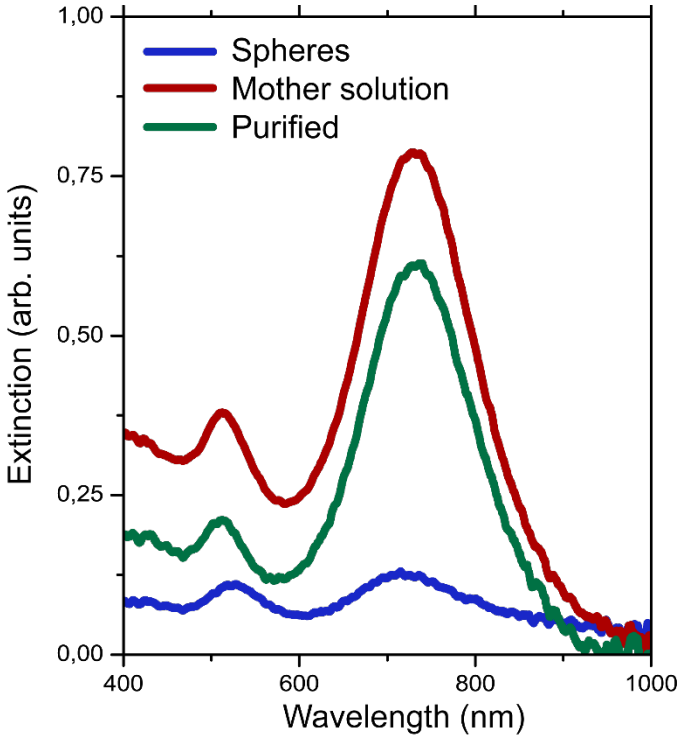


**Figure S2. Extinction spectra of purified low–aspect-ratio gold nanorods.** The extinction spectra of gold nanorods after purification of the low aspect ratio samples provide insights into their shape purity, as indicated by decreased longitudinal-to-transverse plasmon resonance intensity ratios and a slight blueshift in the transverse plasmon resonance band. Mother solution is the colloidal solution before the purification process.

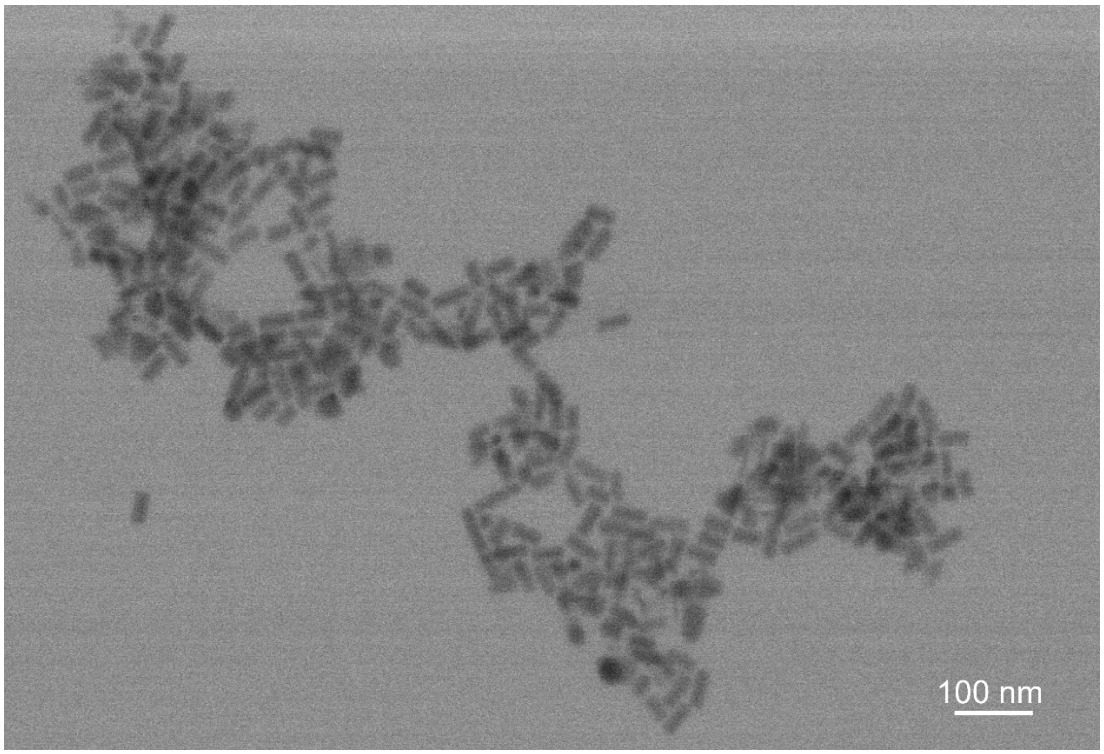


**Figure S3. Large-area STEM images of bimetallic nanocuboids**. Synthesized nanocuboids exhibit high monodispersity and shape purity.

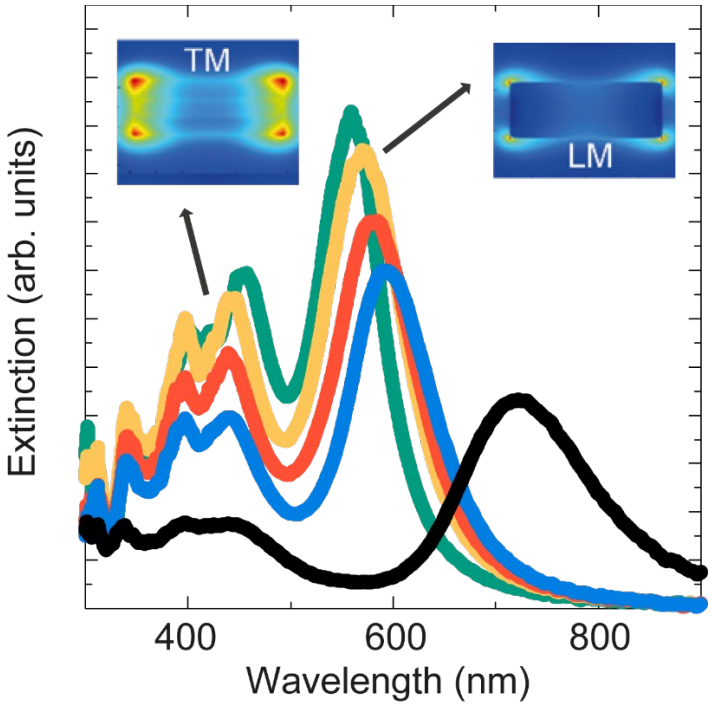


**Figure S4. Plasmonic modes in bimetallic core–shell nanocuboids.** The extinction spectrum details the growth process, where increasing silver nitrate ($AgNO_3$) concentration in the growth solution thickens the silver shell. This thickening causes a blue shift in the longitudinal mode (LM). Meanwhile, the broad transverse mode (TM) near 400 nm splits into two distinct modes and then redshifts as the shell grows thicker. Electric field analysis obtained using Lumerical shows the longitudinal mode is localized at the nanocuboid corners, whereas the transverse mode exhibits strong far-field radiation, indicating enhanced coupling to radiative modes. $AgNO_3$ concentration in increasing order is black, blue, red, yellow, and green.

**Table S1. Electric field distribution of Au@Ag nanocuboids**

| Aspect Ratio of Gold Nanorods | Longitudinal Mode | Transverse Mode |
|---|---|---|
| 3 | 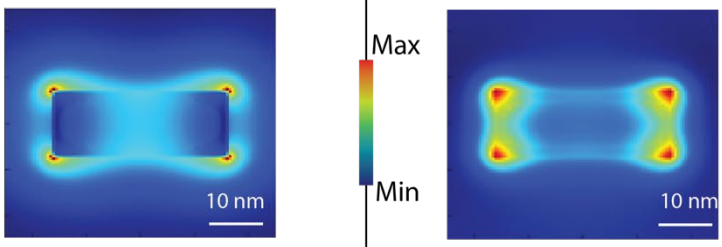  | |
| 4 | 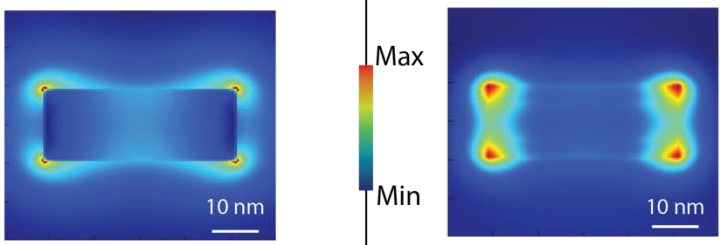  | |
| 5 | 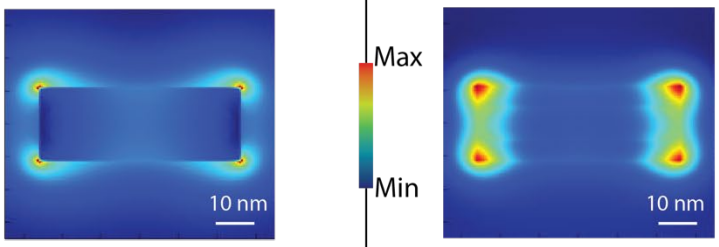  | |
| 6 | 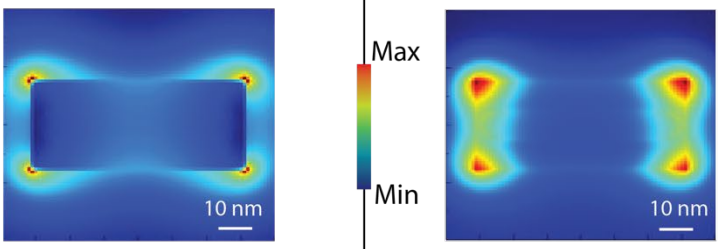  | |
| 7 | 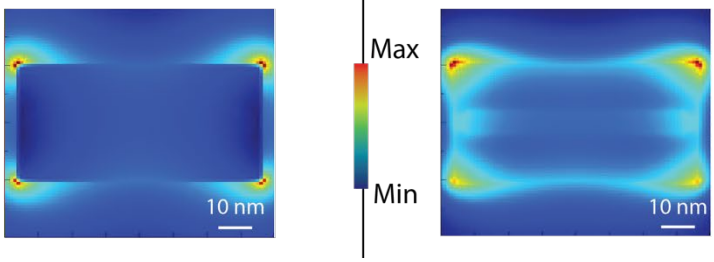  | |

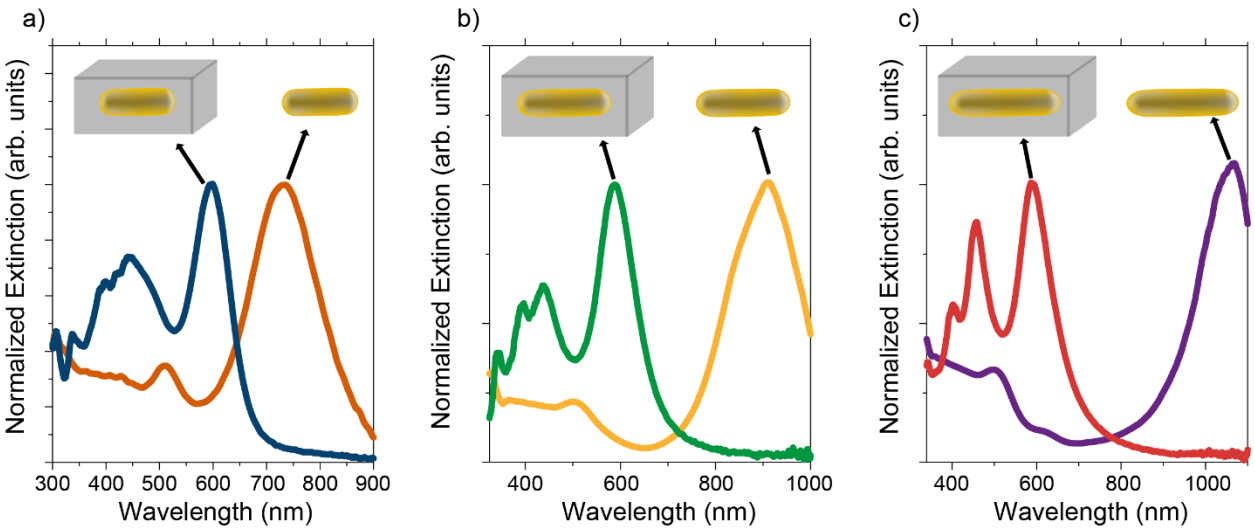


**Figure S5. Aspect-ratio–dependent blue-shift in nanocuboids.** (a–c) show the extinction spectra of bare gold nanorods with mean aspect ratios of 3.6, 5.5, and 7.3, along with their corresponding, blue-shifted bimetallic nanocuboid structures, illustrating tunable plasmonic losses at a fixed wavelength.

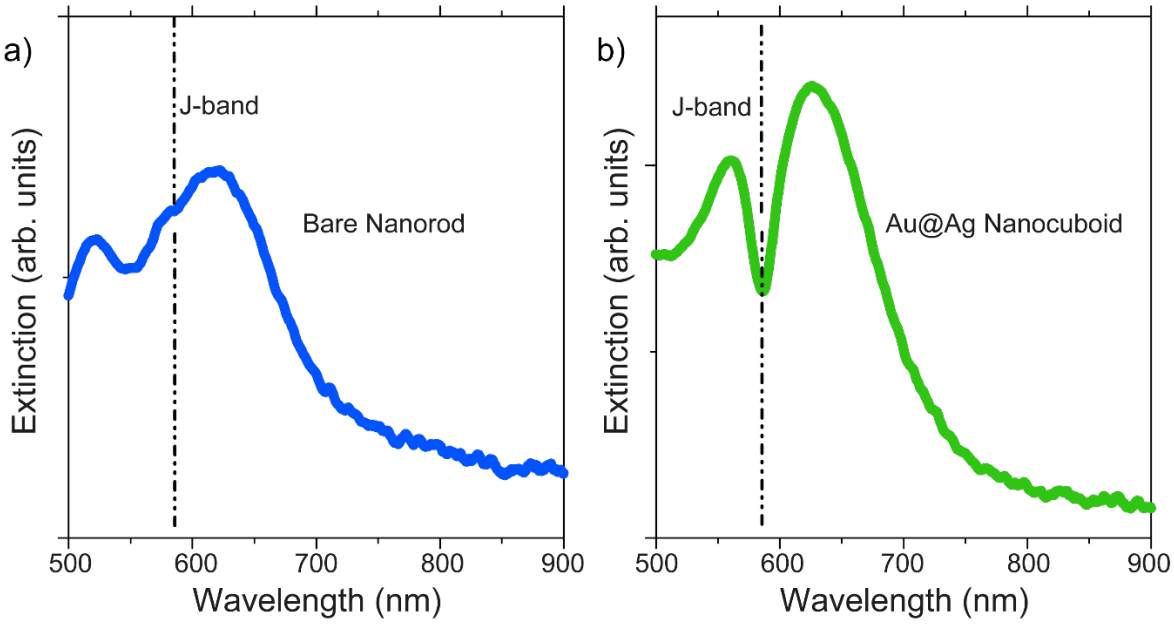


**Figure S6. Morphology-dependent plasmon–exciton coupling at fixed dye concentration.** The addition of a silver shell alters both the morphology and composition of the nanostructure, leading to notable differences in the coupling of bare gold nanorods and bimetallic core–shell nanocuboids with the excitons of J-aggregate dye. These differences arise primarily from enhanced electric field localization at sharp corners and reduced ohmic losses in the nanocuboid structure, attributed to the distinct dielectric properties of silver. Together, these factors enable more efficient plasmon–exciton coupling.

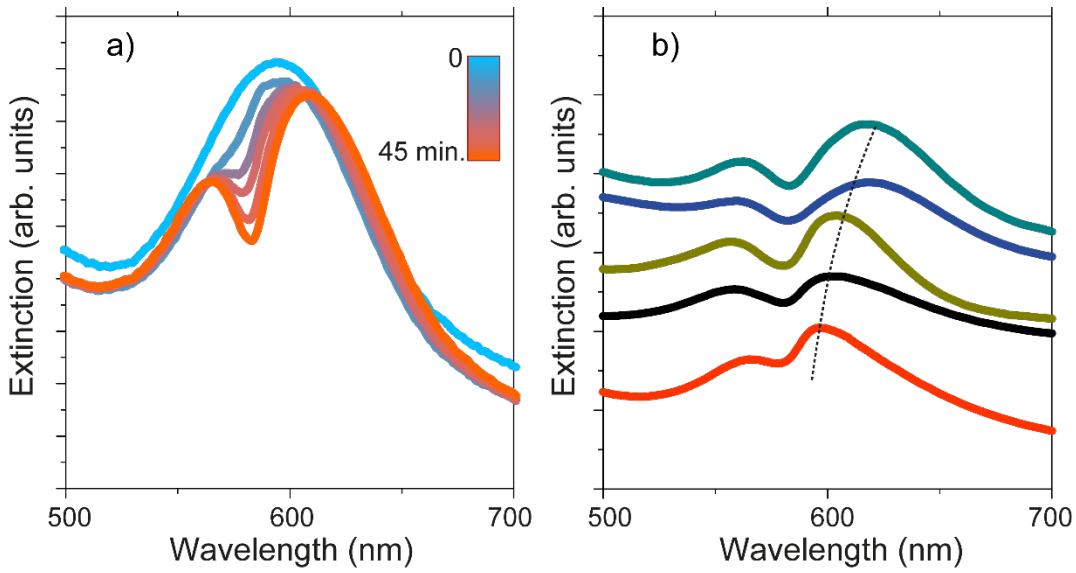


**Figure S7. Time-dependent plexciton formation and effect of aspect-ratio on frequency splitting.** (a) Time-resolved extinction spectra recorded at various intervals after mixing plasmonic nanocuboids with J-aggregates, capturing the progressive self-assembly of excitonic molecules on the nanocuboid surfaces. This process effectively simulates a dye concentration-dependent experiment, as the local exciton population increases over time. (b) Extinction spectra of plexcitonic structures derived from nanocuboids with different monometallic aspect ratios reveal that both the Rabi splitting energies and the depth of the spectral dip vary with monometallic aspect ratio. As the aspect ratio increases, Rabi splitting energies decrease due to an enlarged mode volume, and the spectral dip becomes less pronounced owing to increased radiative losses.

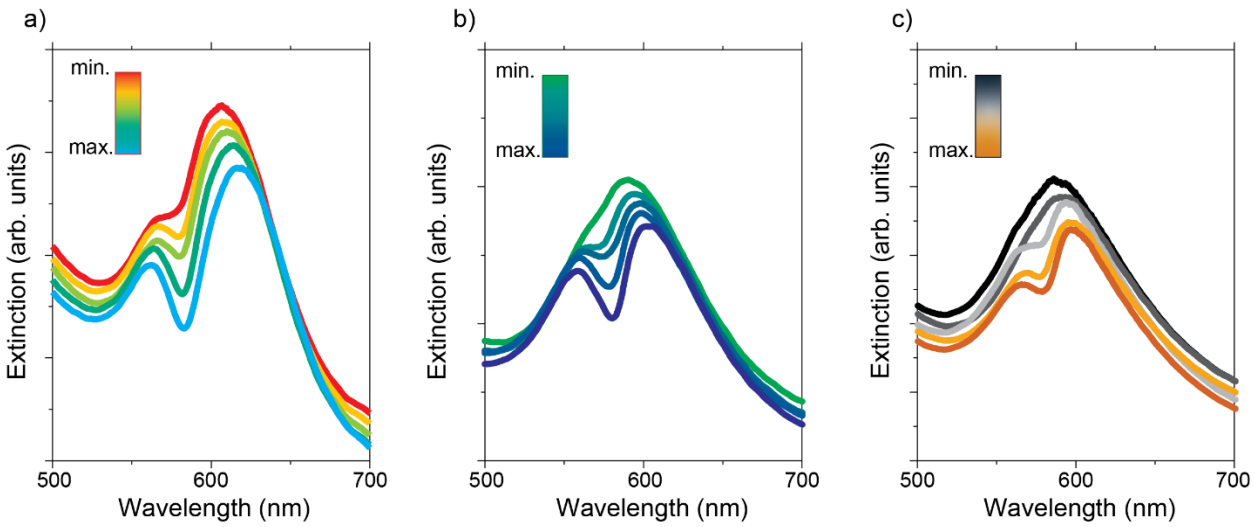


**Figure S8. Plasmon–exciton interaction for nanocuboids with different aspect ratios.** (a–c) present the polaritonic extinction spectra at varying J-aggregate concentrations. The aspect ratio of the bimetallic nanocuboids, as shown in **Fig. S5**, is kept constant to maintain spectral overlap between the plasmon resonance and the excitonic transition of the J-aggregates. The mean aspect ratios of nanorods used in these experiments are 3.6 (left), 5.5, and 7.3 (right). In each panel, J-aggregate concentration value varies between a minimum and maximum. Different colors correspond to different concentrations of J-aggregates.

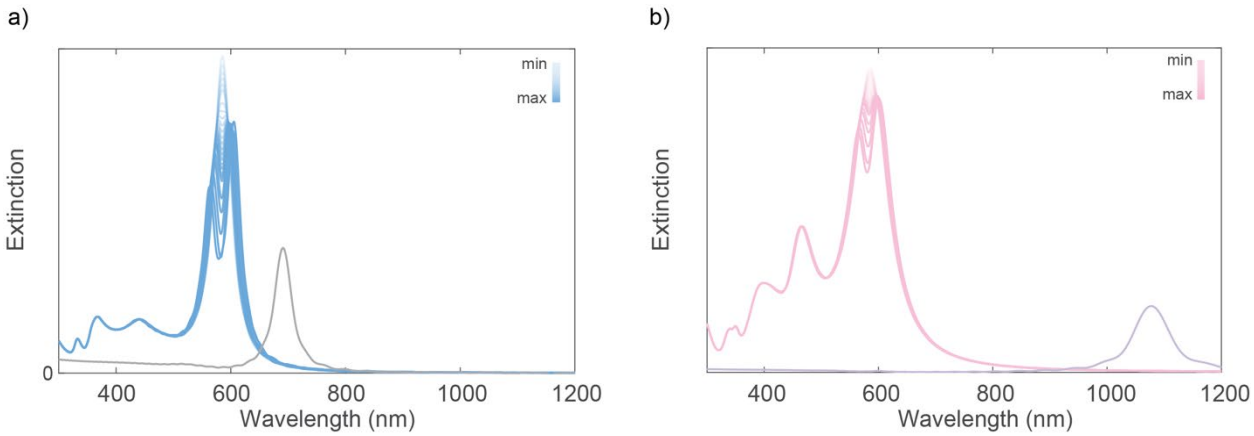


**Figure S9. Aspect-ratio effects on plexciton formation and splitting.** The simulated extinction spectra for gold nanorods with aspect ratios of 3 (a) and 7 (b), along with oscillator strength-dependent plexciton formation, highlight the critical role of plasmonic nanoparticle geometry in governing coupling strength and spectral dip visibility. Nanocuboids with a lower aspect ratio (AR = 3) show stronger Rabi splitting and more distinct spectral dips, while those with a higher aspect ratio (AR = 7) exhibit diminished splitting and less pronounced dips. These differences are attributed to increased mode volume and radiative losses, consistent with the experimental observations in **Fig. S5** and **S8**.

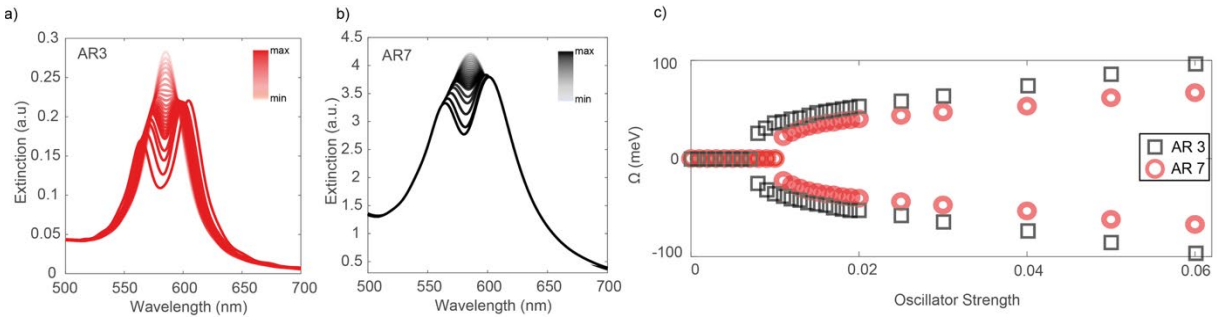


**Figure S10. Aspect-ratio dependence of the position of the EP and the amount of frequency splitting.** Simulation results showing the evolution of EP position as a function of oscillator strength for monometallic nanostructures with aspect ratios of 3 (a) and 7 (b). The EP shifts to higher oscillator strengths as the aspect ratio increases, appearing at approximately 0.006 and 0.011, respectively.

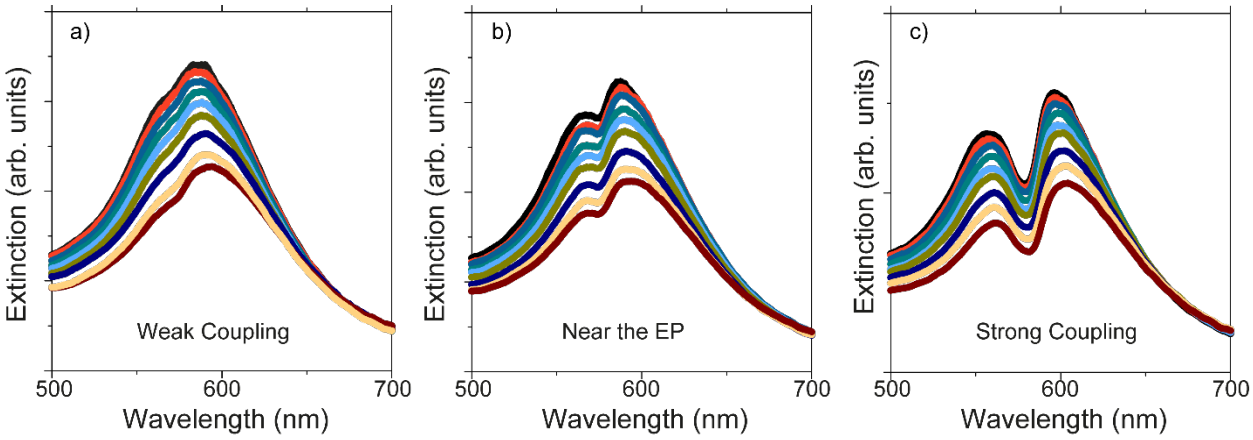


**Figure S11. Refractive-index–induced resonance shifts across coupling regimes.** Refractive-index–dependent spectral measurements performed at different dye concentrations to represent distinct coupling regimes. The surrounding refractive index was varied from 1.333 to 1.382, and the corresponding resonance wavelength shifts were extracted for (a) weak coupling, (b) near-EP, and (c) strong coupling conditions. The largest resonance shift for a small refractive-index variation is observed near the exceptional point.

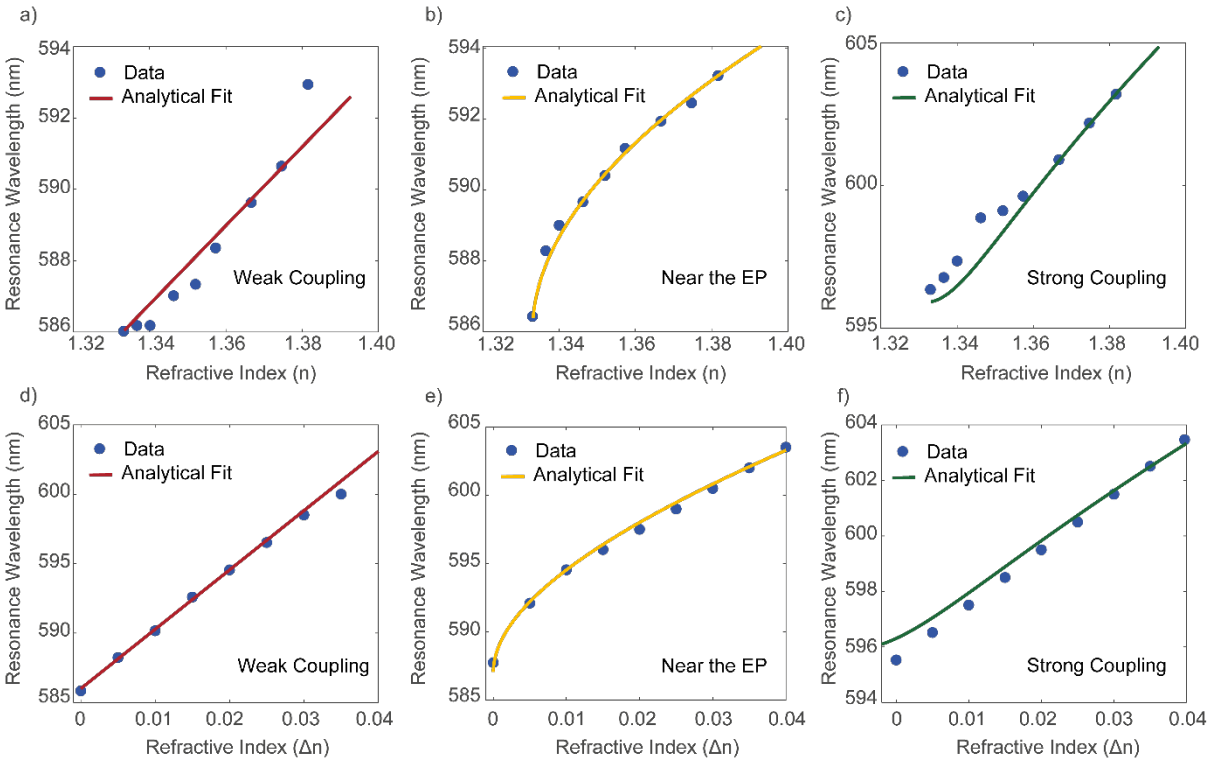


**Figure S12. Refractive index induced shift in the frequency of the brightest resonance peak.** (a–c) Experimental data obtained from spectral maxima of NC4 samples as a function of refractive index. By varying dye concentrations, the NC4 system is set to operate (a) in the weak-coupling, (b) near-EP, and (c) in the strong-coupling regime. (d–f) Corresponding simulations using a monometallic nanocuboid with an aspect ratio of 7. The different coupling regimes are reproduced by modulating the oscillator strength of the dye. Additional simulations investigate the effect of varying the refractive index of the surrounding medium on the optical response. In experimental and simulated datasets, the dependence of the resonance shift on refractive index follows a linear trend in the weak-coupling regime and a square-root–like behavior near the EP, consistent with the splitting analysis (**Fig 5d-f**). In the strong-coupling regime, however, the behavior deviates: while the corresponding splitting exhibits a quadratic dependence (**Fig 5d**), we see that resonance shift can be fitted with a piecewise function, that is linear for large refractive index change and a quadratic function for smaller refractive index changes (see also **Fig. S13, S18, S19**).

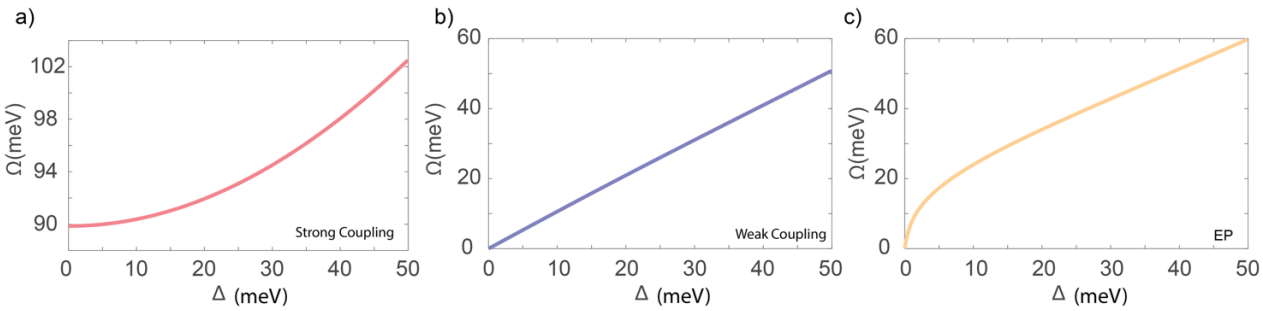


**Figure S13. Theoretical splitting versus plasmon-exciton frequency detuning in different coupling regimes.** Theoretical splitting–detuning curves calculated using coupled-oscillator model under representative (a) weak-coupling, (b) strong-coupling, and (c) EP conditions. Detuning is introduced by sweeping the plasmon resonance while keeping the excitonic resonance fixed, emulating the refractive-index–induced plasmon shift observed experimentally. The resulting trends reveal quadratic (**Fig. 5d**), distinct linear (**Fig. 5e**), and square-root-like (**Fig. 5f**) dependences of mode splitting across the different coupling regimes. Note that in b) there is an initial splitting because the system is in the strong coupling regime. The change in splitting over a detuning of 50meV is 50meV, 12meV, and 60meV respectively for a), b) and c).

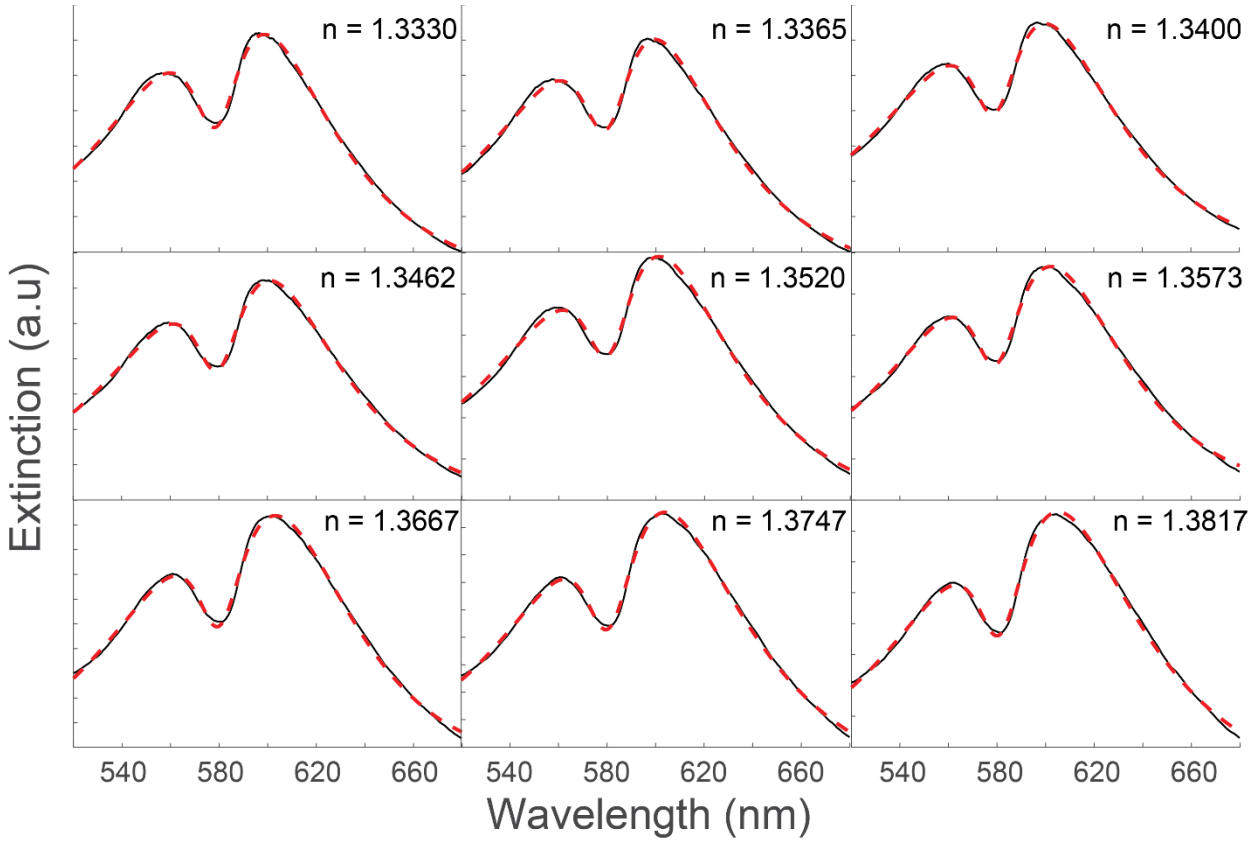


**Figure S14. Refractive index dependent evolution of the plasmon-exciton colloidal system in the strong coupling regime.** Evolution of the extinction spectra of nanocuboids in the strong coupling regime as the refractive index of the colloidal solution (i.e., the surrounding dielectric between LSPR and the TDBC excitons) is varied between 1.3330 and 1.3817 by adding DMSO. As the refractive index increases, the plasmon resonance redshifts, dynamically modifying the plasmon–exciton detuning and resulting in pronounced hybrid mode formation characterized by clear upper and lower polariton branches. Black solid lines represent the experimental (raw) extinction data, while red dashed lines correspond to baseline-corrected fitting results obtained using the two coupled-oscillator model (Equation S27). The splitting values extracted from these fits are presented and discussed in the main text (**Fig. 5d**).

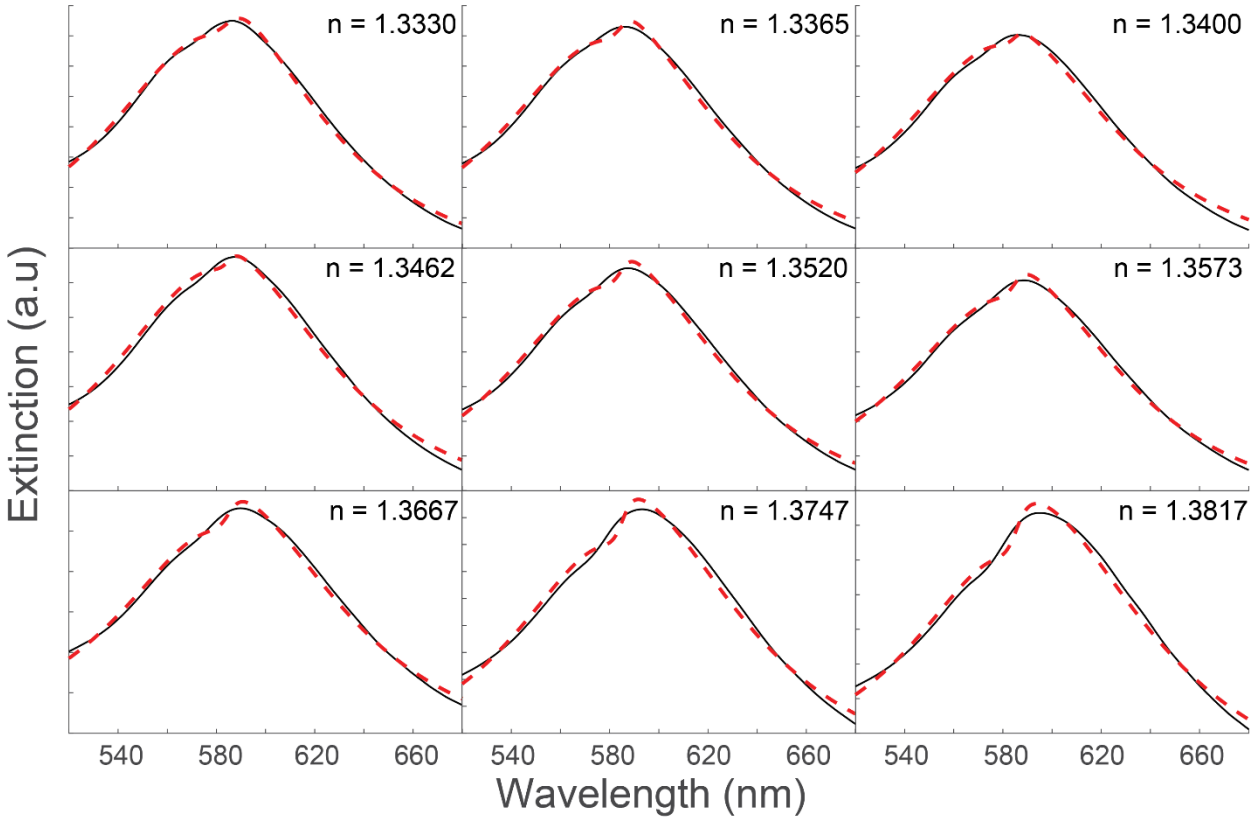


**Figure S15. Refractive index dependent evolution of the plasmon-exciton colloidal system in the weak coupling regime.** Evolution of the extinction spectra of nanocuboids in the weak coupling regime as the refractive index of the colloidal solution (i.e., the surrounding dielectric between LSPR and the TDBC excitons) is varied between 1.3330 and 1.3817 by adding DMSO. Black solid lines represent the experimental (raw) extinction data, while red dashed lines correspond to baseline-corrected fitting results obtained using the two coupled-oscillator model (Equation S27). The gradual spectral shift of the plasmon resonance with increasing refractive index modifies the plasmon–exciton detuning and consequently the hybridization behavior within the weak coupling regime. The splitting values extracted from these fits are presented in the main text (**Fig. 5e**).

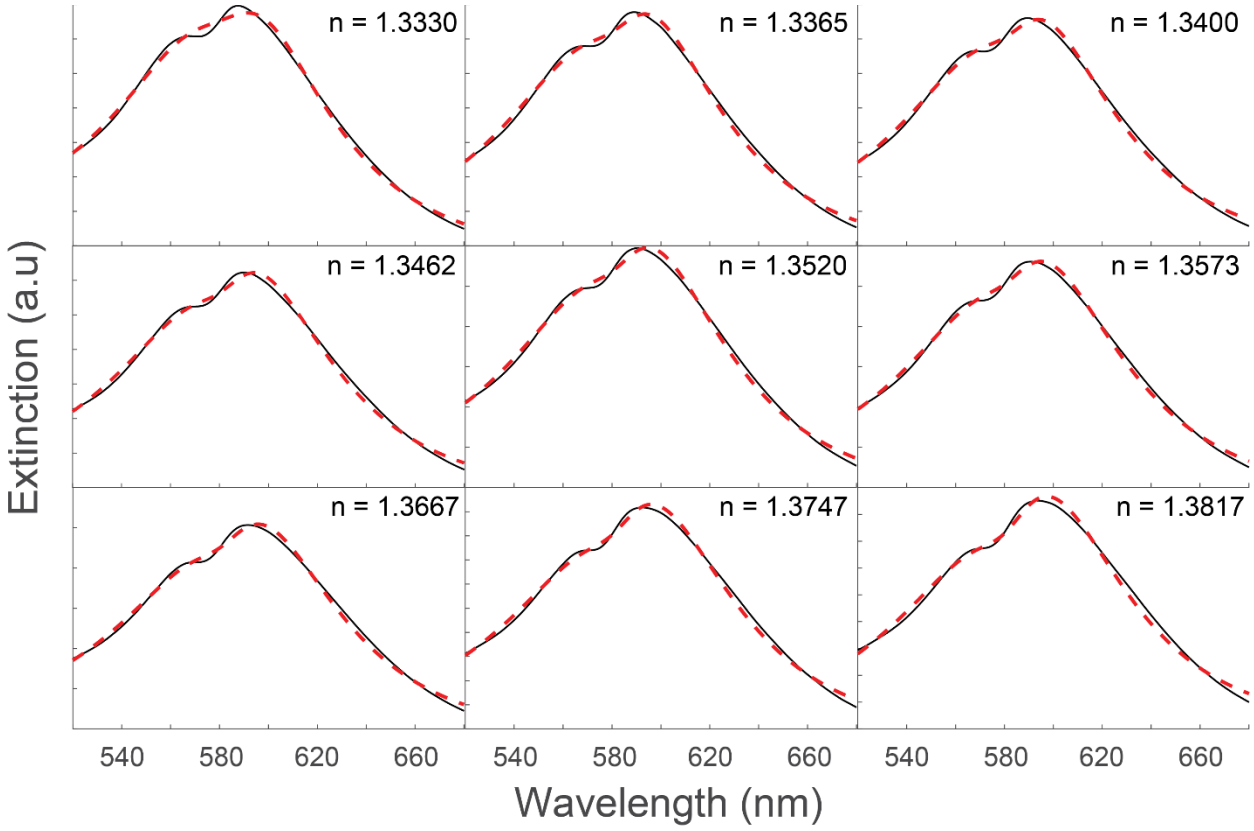


**Figure S16. Refractive index dependent evolution of the plasmon-exciton colloidal system in the vicinity of an EP.** Evolution of the extinction spectra of nanocuboids when the system is initially set in the vicinity of an EP and the refractive index of the colloidal solution (i.e., the surrounding dielectric between the LSPR and the TDBC excitons) is varied between 1.3330 and 1.3817 by adding DMSO. As the surrounding refractive index increases, the plasmon resonance redshifts and tunes the plasmon–exciton detuning toward the EP, where mode coalescence and linewidth redistribution become prominent. The transition from discernible hybrid branches to spectral merging behavior reflects the EP-driven dynamics of the system. Black solid lines represent the experimental (raw) extinction data, while red dashed lines correspond to baseline-corrected fitting results obtained using the two coupled-oscillator model (Equation S27). The splitting values extracted from these fits are presented and analyzed in the main text (**Fig. 5f**).

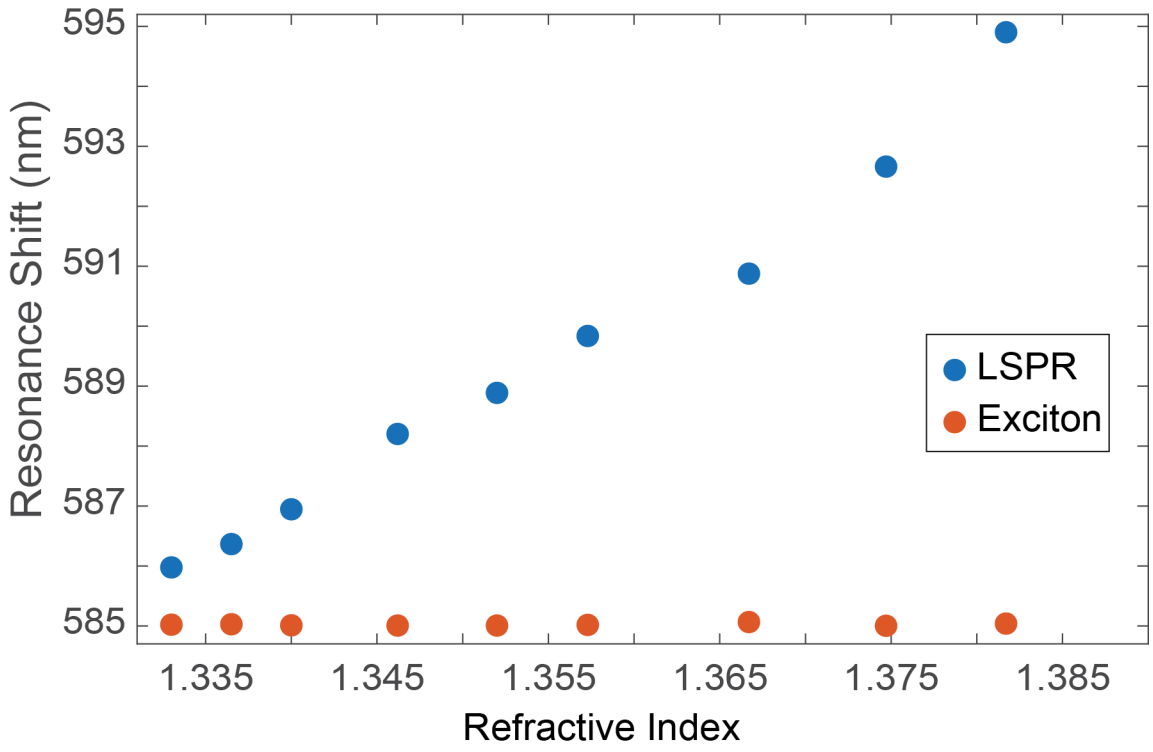


**Figure S17. Refractive index response of uncoupled LSPR and exciton resonances extracted from experimental data.** Resonance positions of the LSPR (blue circles) and TDBC exciton (red circles) as a function of refractive index, obtained from the two coupled-oscillator model fits in the weak coupling regime. The LSPR resonance exhibits a pronounced redshift with increasing refractive index, reflecting its strong sensitivity to changes in the surrounding dielectric environment. In contrast, the exciton resonance remains nearly constant, indicating its weak dependence on the external refractive index. These results highlight the detuning-driven evolution of the plasmon–exciton system and confirm that the refractive index variation predominantly affects the plasmonic mode.

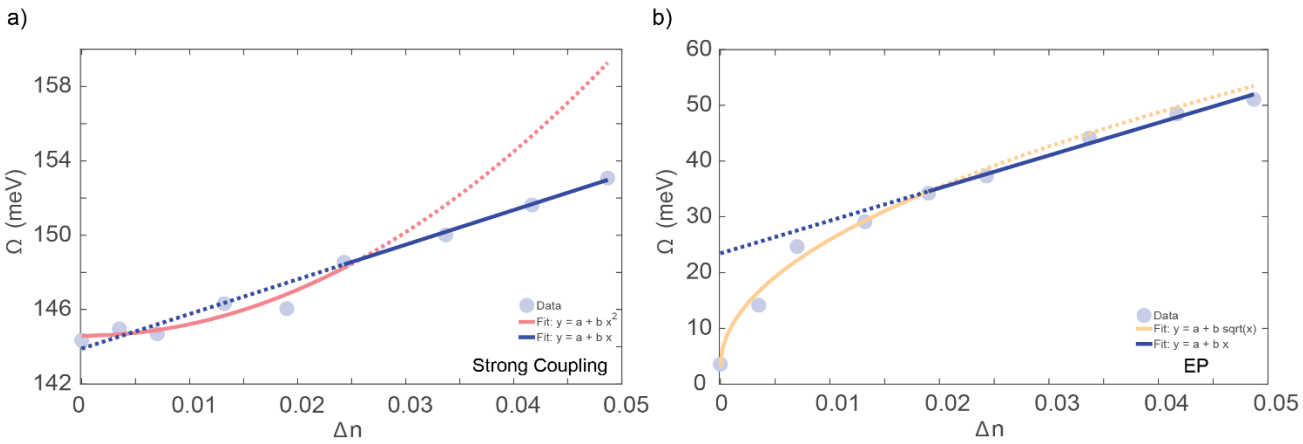


**Figure S18. Mode splitting Ω versus refractive-index perturbation $\Delta n$, with separate fits applied before and after the onset of linear behavior when the system is initially set in the (a) strong coupling and (b) at an EP.** Circles denote the mode splitting extracted from experimentally obtained data, blue lines are linear fit, red curve is a quadratic fit, and yellow curve is a square-root fitting (see Table S2). When the perturbation $\Delta n$ is small, splitting exhibits quadratic scaling in the strong coupling regime and square-root scaling at an EP. When $\Delta n$ is large, mode splitting scales linearly with $\Delta n$ both in the strong coupling regime and at an EP.

**Table S2. Scaling behavior of the splitting response $\Omega(\varepsilon)$ in weak coupling, exceptional point, and strong coupling regimes.**

| | Fit Model | b | $\chi(\varepsilon)$ | Fit Quality ($R^2$) |
|---|---|---|---|---|
| **Weak Coupling** | $\Omega(\varepsilon) = a + b\varepsilon$ <br> $\chi(\varepsilon) = \left\|\frac{d\Omega(\varepsilon)}{2d\varepsilon}\right\|^2 = \frac{b^2}{4}$ | 633.9 | 100457 .31 | 0.983 |
| **Exceptional Point** | $\Omega(\varepsilon) = a + b\sqrt{\varepsilon}$ <br> $\chi(\varepsilon) = \left\|\frac{d\Omega(\varepsilon)}{2d\varepsilon}\right\|^2 = \frac{b^2}{16\varepsilon}$ | 218.8 | $\frac{2992.09}{\varepsilon}$ | 0.993 |
| **Strong Coupling** | $\Omega(\varepsilon) = a + b(\varepsilon)^2$ <br> $\chi(\varepsilon) = \left\|\frac{d\Omega(\varepsilon)}{2d\varepsilon}\right\|^2 = b^2\varepsilon^2$ | 3664 .4 | 13427827 .36 $\varepsilon^2$ | 0.950 |

The response enhancement factor is defined as $\chi(\varepsilon) = \left|\frac{d\Omega(\varepsilon)}{2d\varepsilon}\right|^2$, as introduced in Kononchuk et al.[18] The parameter $b$ is obtained from fits to the measured mode splitting, and $R^2$ indicates the goodness of fit.

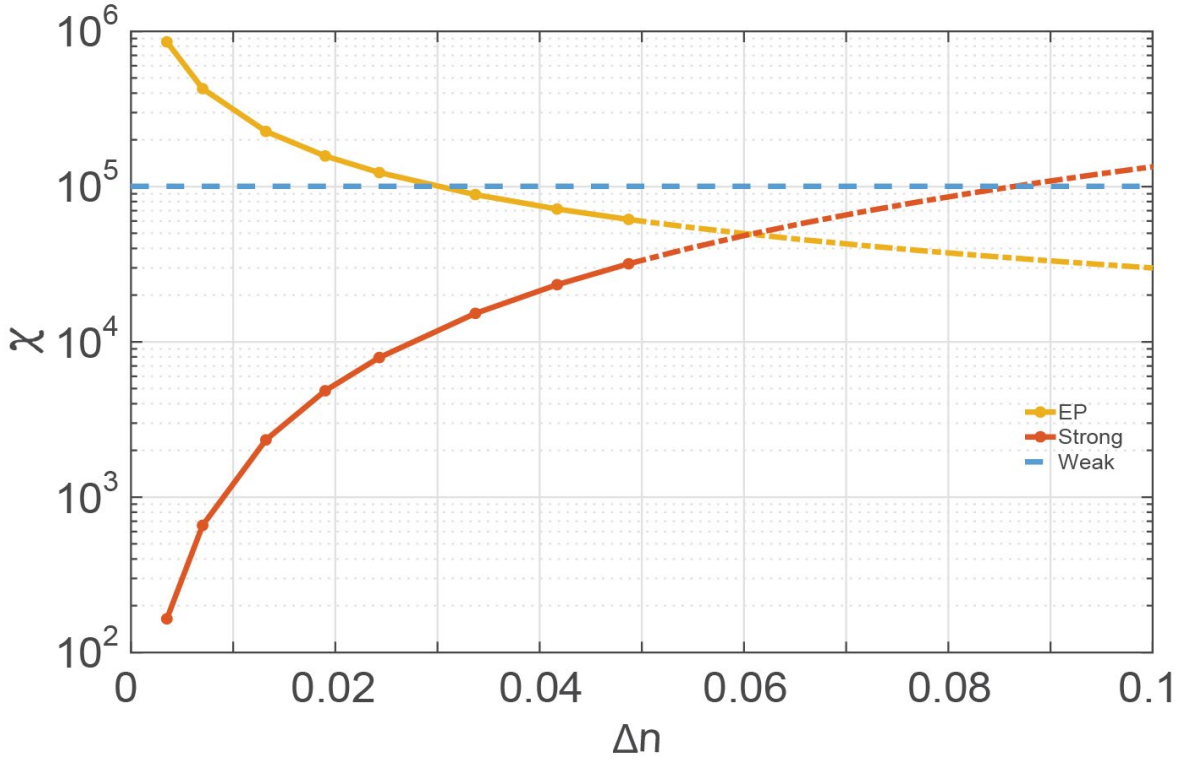


**Figure S19. Response enhancement factor $\chi$ vs. refractive-index perturbation $\Delta n$.** Using the values listed in **Table S2**, the response enhancement factor $\chi$ was calculated as a function of the refractive-index change. For small index perturbations, the exceptional-point (EP) regime exhibits the highest enhancement. However, as also seen in **Fig. S18b**, when the index changes approaches $\sim 0.03$, the EP response begins to follow a behavior similar to the linear trend of the weak-coupling regime. A comparable transition for the strong-coupling case appears only at larger index variations, as also seen in **Fig. S18a**.

## REFERENCES


1 Nikoobakht, B. & El-Sayed, M. A. Preparation and growth mechanism of gold nanorods (NRs) using seed-mediated growth method. *Chemistry of materials* **15**, 1957-1962 (2003).

2 Burrows, N. D., Harvey, S., Idesis, F. A. & Murphy, C. J. Understanding the seed-mediated growth of gold nanorods through a fractional factorial design of experiments. *Langmuir* **33**, 1891-1907 (2017).

3 Lohse, S. E. & Murphy, C. J. The quest for shape control: a history of gold nanorod synthesis. *Chemistry of Materials* **25**, 1250-1261 (2013).

4 Gole, A. & Murphy, C. J. Seed-mediated synthesis of gold nanorods: role of the size and nature of the seed. *Chemistry of Materials* **16**, 3633-3640 (2004).

5 Ye, X., Zheng, C., Chen, J., Gao, Y. & Murray, C. B. Using binary surfactant mixtures to simultaneously improve the dimensional tunability and monodispersity in the seeded growth of gold nanorods. *Nano letters* **13**, 765-771 (2013).

6 Vigderman, L. & Zubarev, E. R. High-yield synthesis of gold nanorods with longitudinal SPR peak greater than 1200 nm using hydroquinone as a reducing agent. *Chemistry of Materials* **25**, 1450-1457 (2013).

7 Rayavarapu, R. G., Ungureanu, C., Krystek, P., Van Leeuwen, T. G. & Manohar, S. Iodide impurities in hexadecyltrimethylammonium bromide (CTAB) products: lot− lot variations and influence on gold nanorod synthesis. *Langmuir* **26**, 5050-5055 (2010).

8 Smith, D. K. & Korgel, B. A. The importance of the CTAB surfactant on the colloidal seed-mediated synthesis of gold nanorods. *Langmuir* **24**, 644-649 (2008).

9 Boksebeld, M., Blanchard, N. P., Jaffal, A., Chevolot, Y. & Monnier, V. Shape-selective purification of gold nanorods with low aspect ratio using a simple centrifugation method. *Gold Bulletin* **50**, 69-76 (2017).

10 Scaletti, F., Kim, C. S., Messori, L. & Rotello, V. M. Rapid purification of gold nanorods for biomedical applications. *MethodsX* **1**, 118-123 (2014).

11 Liu & Guyot-Sionnest, P. Synthesis and optical characterization of Au/Ag core/shell nanorods. *The Journal of Physical Chemistry B* **108**, 5882-5888 (2004).

12 Jiang, R., Chen, H., Shao, L., Li, Q. & Wang, J. Unraveling the evolution and nature of the plasmons in (Au core)–(Ag shell) nanorods. *Advanced Materials* **24**, OP200 (2012).

13 Balci, S. *et al.* Tunable Plexcitonic Nanoparticles: A Model System for Studying Plasmon-Exciton Interaction from the Weak to the Ultrastrong Coupling Regime. *Acs Photonics* **3**, 2010-2016 (2016). https://doi.org/10.1021/acsphotonics.6b00498

14 Liang, K., Guo, J., Huang, Y. & Yu, L. J. N. Fine-tuning of polariton energies in a tailored plasmon cavity and J-aggregates hybrid system. **12**, 23069-23076 (2020).

15 Palik, E. D. *Handbook of optical constants of solids*. Vol. 3 (Academic press, 1998).

16 Oughstun, K. E. & Cartwright, N. A. On the Lorentz-Lorenz formula and the Lorentz model of dielectric dispersion. *Optics Express* **11**, 1541-1546 (2003). https://doi.org/10.1364/Oe.11.001541

17 Limonov, M. F., Rybin, M. V., Poddubny, A. N. & Kivshar, Y. S. Fano resonances in photonics. *Nat Photonics* **11**, 543-554 (2017). https://doi.org/10.1038/Nphoton.2017.142

18 Kononchuk, R., Cai, J., Ellis, F., Thevamaran, R. & Kottos, T. Exceptional-point-based accelerometers with enhanced signal-to-noise ratio. *Nature* **607**, 697-702 (2022).